

# Large Intestine 3D Shape Refinement Using Point Diffusion Models for Digital Phantom Generation

Kaouther Mouheb, Mobina Ghoghgh Nejad, Lavsén Dahal, Ehsan Samei, Kyle J. Lafata, W. Paul Segars, and Joseph Y. Lo

arXiv:2309.08289v2 [cs.CV] 20 May 2024

**Abstract**— Accurate 3D modeling of human organs plays a crucial role in building digital phantoms for medical imaging research and virtual imaging trials. However, generating anatomically plausible organ surfaces from computed tomography scans remains challenging for many structures, particularly the large intestine. In this study, we propose CLAP, a Conditional LATent Point-diffusion model leveraging recent advancements in geometric deep learning and denoising diffusion probabilistic models to refine the segmentation results of the large intestine. We begin by representing the organ as point clouds sampled from the surface of the 3D segmentation mask. Subsequently, we employ a hierarchical variational autoencoder to obtain global and local latent representations of the organ’s shape. Two conditional denoising diffusion models are trained in the hierarchical latent space to perform shape refinement. To further enhance CLAP, we incorporate a state-of-the-art surface reconstruction model, allowing us to generate smooth meshes from the complete point clouds. Experimental results demonstrate the effectiveness of our approach in capturing both the global distribution of the organ’s shape and its fine details. Our complete refinement pipeline demonstrates substantial enhancements in surface representation compared to the initial segmentation, reducing the Chamfer distance by 70% and the Hausdorff distance by 32%. By combining geometric deep learning, denoising diffusion models, and advanced surface reconstruction techniques, our proposed method offers a promising solution for accurately modeling the large intestine’s surface and can potentially be extended to other anatomical structures.

**Index Terms**— Digital Phantom, Denoising Diffusion Models, Geometric Deep Learning, Large Intestine Modeling, 3D Shape Refinement.

## I. INTRODUCTION

**I**N virtual imaging trials, realistic digital phantoms are crucial because they serve as virtual patients. Together with

This research was supported by the EMJMD in Medical Imaging and Applications (MAIA) funded by the European Commission, NIH/NIBIB P41-EB028744, and NIH/NCI R01-CA261457.

Kaouther Mouheb was with the Center for Virtual Imaging Trials, Department of Radiology, Duke University School of Medicine. She is now with the Biomedical Imaging Group Rotterdam of Erasmus Medical Center, Rotterdam, Netherlands (k.mouheb@erasmusmc.nl).

Mobina Ghoghgh Nejad, Lavsén Dahal, Ehsan Samei, Kyle J. Lafata, W. Paul Segars and Joseph Y. Lo are with the Center for Virtual Imaging Trials, Department of Radiology, Duke University School of Medicine, Durham, NC, USA.

simulations of image acquisition and diagnostic interpretation, digital phantoms allow researchers to conduct rigorous experiments with myriad parameter combinations, while obviating concerns about the high costs of trials and excessive radiation exposure [1]–[3]. A typical pipeline of creating computational patient models involves segmenting multiple organs from patient imaging data, then converting the resulting masks into deformable mathematical representations like polygon meshes [4]. Segmentation is a crucial initial step that greatly influences the quality of the generated phantoms. Early studies relied on manual contouring [4] or conventional image processing-based algorithms [5]. Recent deep learning (DL) segmentation algorithms have leveraged access to large datasets to segment multiple organs from computed tomography (CT) scans [6], [7]. Notably, TotalSegmentator [8] achieved state-of-the-art segmentation of approximately 100 organs or structures. Even though these methods significantly outperform their traditional counterparts, the segmentation of many important organs remains quite challenging [9].

Segmentation is particularly challenging for the large intestine, often yielding disconnected surfaces (over-segmentation) or incorporating sections of adjacent organs such as the small intestine or stomach (under-segmentation). These issues stem from two main factors. First, segmenting the large intestine is a very complex task. Consider that this low-contrast, soft-tissue organ is surrounded by other such soft-tissue abdominal organs. The intestines have diverse shape and size that vary greatly among patients. The shape is further impacted by heterogeneous filling with food waste, air, and even exogenous contrast material. [10]. Second, current DL algorithms, such as U-Nets [11], rely on volumetric Convolutional Neural Networks (CNNs), which produce discrete voxel grids that do not account for shape constraints. This voxelization leads to discretization effects when converted to surface representations, ultimately resulting in shapes that may be anatomically inaccurate [12], [13]. Manually correcting these shapes is laborious, time-consuming, and subjective, which highlights the necessity for an automated approach that produces anatomically acceptable shapes.

3D shape completion and refinement has been extensively studied in various domains, including autonomous driving, robotics, and manufacturing [14], [15]. In these fields, LiDAR sensors are frequently employed to detect objects, leading to

sparse, noisy, and partial shapes represented as point clouds. To address the need for shape completion, denoising, and refinement of such complex 3D data, a notable advancement was the introduction of geometric deep networks such as PointNets [16]. Unlike traditional CNNs that operate on volumetric data, PointNets are explicitly designed for processing point cloud data, enabling more efficient and effective analysis of 3D shapes and surfaces. The use of such geometric models has been explored in medical imaging for different tasks [12], [17]. Balsiger et al. [18] used a point cloud-based approach to refine peripheral nervous system segmentations. After initial segmentations by CNN, point clouds were extracted from the mask’s surface and their xyz-coordinates were combined with the deep image features. Using a PointCNN [19], each point was classified as foreground or background to refine the segmentation and eliminate noise. Although this approach effectively addressed false positives, it did not recover false negatives overlooked by the segmentation network. Recently, denoising diffusion probabilistic models (DDPMs) [20] were demonstrated to complete missing data for 1D signals like speech, 2D representations like images, and 3D structures such as object shapes [21]–[23]. An example application of diffusion models for 3D shape generation was the latent Point Diffusion Model (LION) [24], which employed a variational autoencoder (VAE) with a hierarchical latent space to combine global and local representations. By training DDPMs in this smoother latent space, the model captured shape distributions and generated higher-quality shapes. LION achieved state-of-the-art performance on benchmarks and can be extended to other applications like text-to-shape generation. For shape completion, the Point Diffusion-Refinement (PDR) approach comprised a Conditional Generation Network (CGNet) and a Refinement Network (RFNet) [25]. CGNet is a conditional DDPM, generating a coarse but complete point cloud from partial input, while RFNet densifies the point cloud for quality improvement. Both networks utilize a dual-path architecture based on PointNet++ [26] for efficient feature extraction from partial shapes and precise manipulation of 3D point locations. For medical imaging, Friedrich et al. [27] applied point diffusion models by using point-voxel diffusion (PVD) [23] to propose implants that complete defective skull shapes. This approach effectively generated missing false negative points, but it could not remove false positive points that remained fixed throughout the diffusion process.

In this research, we aim to address the issue of inaccurate surface reconstructions of the large intestine resulting from a volumetric segmentation model by leveraging the latest advancements in geometric deep learning and DDPMs. Distinct from Balsiger et al. [18], our approach incorporates generative geometric models capable of generating new points to fill in the missing parts of the organ’s shape representation. To tackle false positives, we extract features from the suboptimal shapes to guide the refinement. In contrast to Friedrich et al. [27], we do not fix the shapes during the diffusion process. Rather, we represent the shapes as point clouds and employ latent denoising diffusion models with PointNet-based backbones, conditioned on the partial shapes of the organ, to output shapes that are complete. Additionally, we employ a modern surface

reconstruction method to represent the final outputs as polygon meshes, which is a preferred representation in computational phantoms. The contributions of this work can be summarized as follows:

- To the best of our knowledge, we are the first to tackle the problem of large intestine shape refinement as a conditional point cloud generation task.
- We construct a dataset consisting of pairs of 3D large intestine shapes. Each pair includes a suboptimal shape and the corresponding reference standard.
- Building on LION [24] and PDR [25], we introduce a novel method for point cloud refinement, which involves training conditional point-diffusion models within a hierarchical latent space.
- We propose a simple post-processing pipeline for point clouds that effectively increases density and smooths out noise before performing surface reconstruction.

## II. MATERIAL AND METHODS

In this section, we first describe the dataset generation procedure. Subsequently, we present the baseline approach followed by our novel method, specifically designed to enhance and optimize the results. Finally, we detail the post-processing and surface reconstruction pipeline.

### A. Dataset

We created a dataset that includes pairs of suboptimal and corrected 3D shapes of the large intestine. Our data include one public and two private datasets.

1) *TotalSegmentator Dataset*: Wasserthal et al. [8] provided a public dataset of 1024 CT scans with reference masks for the large intestine (referred to as "colon"). The dataset contains various CT types, some of which lack the large intestine entirely (e.g., head CTs) or only contain parts of it. We established the following rules to extract cases with complete large intestines based on connected component analysis and the organ volume distributions derived from the provided reference masks:

- Cases with a stomach volume lower than 50ml and a urinary bladder volume of 0ml are eliminated, thus ensuring the upper and lower bounds of the intestine are present.
- Outlier cases with large intestine volume lower than 400ml or higher than 1500ml are eliminated.
- Volumes were analyzed to ensure the presence of two distinct connected components (representing the large intestine and the background). In instances where the organ was fragmented, binary closing operations were applied to merge the fragments, ensuring the organ’s connectivity.
- After the binary closing, only the cases with two connected components are kept.

The number of remaining cases after the selection process is 308.

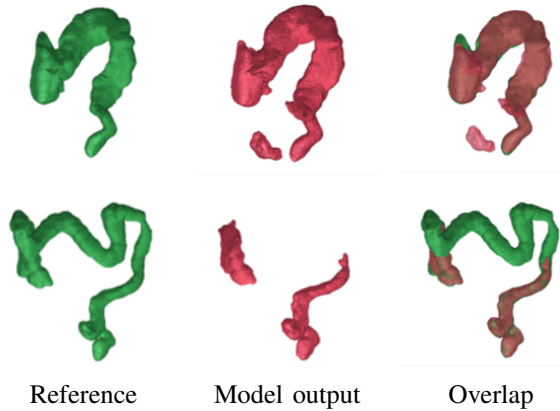


Fig. 1: Examples of suboptimal TotalSegmentator results with the corresponding references annotated by a physician. The segmentation failures include false positives included from other organs (upper row) and missing components (lower row).

2) *Duke PET/CT Dataset*: This set comprises 112 diagnostic-quality CT volumes from Positron Emission Tomography and Computed Tomography (PET/CT) scans performed at Duke Health. TotalSegmentator’s pre-trained model was applied to segment the large intestine. Further analysis for extracting the successful cases involved noise removal and applying binary closing to address minor disconnections. After excluding cases with more than two components, there were 75 remaining cases.

3) *Duke CAP Dataset*: The set includes 269 Chest Abdomen Pelvis (CAP) CT scans from Duke Health patients. The samples underwent the same pipeline as the PET/CT cases. Additionally, a physician refined 34 cases with incorrect masks resulting in a total of 195 cases.

4) *Partial Shape Synthesis*: To refine organ shapes within a supervised learning framework, we needed cases with initial shape inaccuracies as inputs, and paired them with their correctly shaped counterparts for output targets. In a controlled process, the previously curated shapes were used to create suboptimal input masks with the appearance of less desirable cases often found in public datasets, as illustrated in fig. 1. For this purpose, we built an under-trained 3D, full-resolution nn-Unet [28] using only 30 epochs and 30 images randomly selected from our TotalSegmentator subset. We ran inference using this model on all cases in our dataset to obtain the suboptimal segmentation masks.

5) *Point Cloud Extraction*: Given the pairs of suboptimal and reference masks, the marching cubes algorithm [29] was used to extract the organ surfaces represented as polygon meshes. Using Poisson disk sampling [30], point clouds of 2048 points were extracted from those surface meshes. Finally, the dataset was normalized globally to  $[-1, 1]$  using the mean and standard deviation calculated over all shapes in the training set.

We split the data into approximately 70% for training, 10% for validation, and 20% for testing. The final numbers of shapes in each set after the split are summarized in table I.

	TotalSeg	PET/CT	CAP	Total
Train	216	55	134	405
Validation	32	6	23	61
Test	60	14	38	112
Total	308	75	195	578

TABLE I: Dataset final shape counts and split.

## B. Problem Statement

We formulated our task as conditional 3D shape generation. A 3D point cloud sampled from the surface of a segmentation mask is represented by  $N$  points with xyz-coordinates in the 3D space:  $x \in \mathbb{R}^{N \times 3}$ . We assumed the dataset  $\mathcal{D}$  is composed of  $M$  data pairs  $\{(x^i, c^i) | 1 \leq i \leq M\}$ , where  $x^i$  is the  $i^{th}$  reference point cloud and  $c^i$  is the corresponding suboptimal point cloud of the organ’s surface. The goal was to create a conditional model that generates a complete shape  $y^i$  that represents an anatomically plausible shape of a large intestine, using the input  $c^i$  as a conditioner. Note that the generated shape  $y^i$  is as close as possible but does not necessarily match the reference shape  $x^i$ .

## C. Baseline: Conditional Generation Network

We used our dataset to train the Conditional Generative Network (CGNet) of PDR [25] to serve as our baseline. Assuming  $p_{intestine}$  is the distribution of the complete large intestine shapes  $x^i$  and  $p_{latent}$  is the latent distribution representing a standard Gaussian in  $\mathbb{R}^{N \times 3}$ , CGNet is designed as a DDPM that consists of two processes:

- **Forward diffusion**: a Markov chain that adds noise gradually to the clean data distribution  $p_{intestine}$  using Gaussian kernels of fixed variances in  $T$  time steps. Variances are fixed such that at the final step  $T$ , the shapes belong to the standard Gaussian distribution  $p_{latent}$ . This process does not depend on the conditioner.
- **Reverse diffusion**: a Markov chain implemented as a neural network based on an encoder-decoder architecture with PointNet++ [26] backbone. The model predicts the noise added during the forward process. This process is conditioned on the suboptimal shape  $c$ . It starts with a sample  $x_T$  from  $p_{latent}$  and gradually denoises it to obtain a clean shape  $x_0$  from  $p_{intestine}$ .

The time embedding size was set to 128. The number of neighbors  $K$  used for clustering in all PointNet++ layers was set to 10. The number of features of the conditioner (other than the xyz-coordinates) was set to 0. Since there is only a single class, no class conditioning mechanism was used. The model was trained for 8000 epochs with a learning rate of  $5 \times 10^{-4}$  and a batch size of 16. The remaining hyperparameters were set to the defaults defined in PDR [25].

## D. Latent Conditional Point-Diffusion Network

To improve the refinement, we shifted the conditional generation process to a smoother latent space. The inspiration behind this lies in the high complexity and variability of the large intestine’s shapes, making it challenging for the DDPM

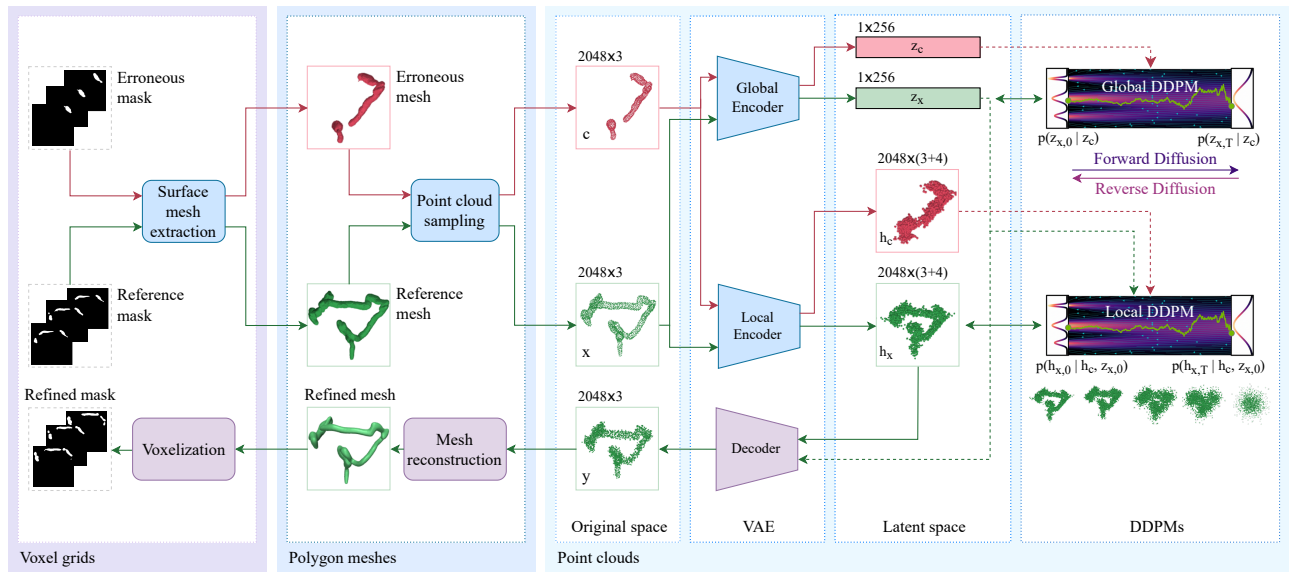


Fig. 2: Latent conditional point cloud refinement framework: surface meshes are extracted from the reference and suboptimal organ masks using the marching cubes algorithm and point clouds are created from both surfaces using Poisson disk sampling. The shapes are encoded into a global and a local representation via two VAE encoders. Two DDPMs are trained to model the distributions of global and local representations of the complete shapes conditioned on the latent representations of the partial shapes. The clean shape is reconstructed to the original space via the VAE’s decoder. After post-processing, Point-E’s deep implicit model is used to reconstruct a polygon mesh that can be voxelized into a 3D mask.

to accurately model their distribution in the original space. Based on Zeng et al. [24], we trained a VAE that encoded both partial and complete shapes into a unified, smoother latent space consisting of a vector-valued global representation and a point cloud-structured local representation. Subsequently, two DDPMs were trained to model the distributions of complete shapes’ latent representations conditioned on the representations of partial shapes. This enabled the disentanglement of high-level features related to the overall appearance of the organ from the low-level features expressing the fine details, making it easier for the DDPMs to model the underlying distributions. Finally, the VAE’s decoder was used to combine both representations to reconstruct the complete shape in the original space. During training, data augmentation was employed using rigid 3D transformations. This included scaling, with a factor of up to 10% of the original size, rotation around the z-axis of up to  $10^\circ$ , and translation of up to 0.1 units in the normalized space. The overall design of our complete framework is illustrated in Fig. 2.

**1) Hierarchical Latent Shape Encoding:** For the latent shape encoding, we adapted the approach from Zeng et al. [24]. Taking a pair of shapes  $(x, c)$  from the training set  $\mathcal{D}$ , a VAE learns a global latent representation  $(z_x, z_c) \in (\mathbb{R}^{D_z})^2$  and a local latent representation  $(h_x, h_c) \in (\mathbb{R}^{N \times (3+D_h)})^2$ . In other words,  $z_x$  and  $z_c$  are 1D vectors of size  $D_z$  whereas  $h_x$  and  $h_c$  are latent point clouds of  $N$  points, each carrying its xyz-coordinates and  $D_h$  additional features. The VAE consisted of two encoders and a decoder all based on the PVCNN architecture [31]. The global encoder converts a 3D point cloud  $s \in \{x, c\}$  into a global latent vector  $z_s$ . The local encoder takes the point cloud  $s$  as input and its global rep-

resentation  $z_s$  as a condition and generates the corresponding local representation  $h_s$ . The VAE’s decoder accepts  $h_s$  as input and  $z_s$  as a condition and reconstructs the shape  $s$  back to the original space. The VAE was trained by maximizing a modified version of the variational lower bound on the data log-likelihood (ELBO) [24].

Hyperparameters were fine-tuned as follows:  $D_z$  was set to 256 and  $D_h$  to 4. The maximum values of both KL weights of the loss function  $\lambda_z$  and  $\lambda_h$  were set to 0.4. To initialize the VAE weights, the variance offset parameter was set to 12 and the skip connections’ weight was set to 0.02. The Adam optimizer was used with batch size of 32 and learning rate of  $10^{-3}$ . The VAE was trained for 6000 epochs. Note that the VAE was trained using both partial and complete shapes since both shapes need to be encoded to the latent space for training the conditional DDPMs.

**2) Latent Conditional Point Generation:** Freezing the VAE weights, we trained two conditional DDPMs in the hierarchical latent space. A first DDPM with parameters  $\xi$  was trained on the global latent encodings  $z_x$  conditioned on  $z_c$ . A second DDPM with parameters  $\phi$  was trained on the local latent encodings  $h_x$  conditioned on both  $h_c$  and  $z_x$ . The models were trained by minimizing the difference between the actual noise added to the reference latent encodings and the noise predicted by the DDPMs. The loss function of the first DDPM can be written as:

$$\mathcal{L}(\xi) = \mathbb{E}_{i \sim \mathcal{U}([M]), t \sim \mathcal{U}([T]), \epsilon \sim \mathcal{N}(0, I)} \|\epsilon - \epsilon_\xi(z_{x,t}^i, t, z_c^i)\|^2 \quad (1)$$

$\mathcal{U}([M])$  represents the uniform distribution over  $\{1, 2, \dots, M\}$ ,  $\mathcal{U}([T])$  represents the uniform distribution over  $\{1, 2, \dots, T\}$ ,  $z_{x,t}^i$  is the diffused global latent representation of the shape

$x^i$  after  $t$  diffusion steps,  $z_c^i$  is the global representation of the corresponding conditioner  $c^i$ ,  $\epsilon$  is the actual noise, and  $\epsilon_\xi$  is the noise predicted by the model.

Similarly, the loss function of the second DDPM is defined as:

$$\mathcal{L}(\phi) = \mathbb{E}_{i \sim \mathcal{U}([M]), t \sim \mathcal{U}([T]), \epsilon \sim \mathcal{N}(0, I)} \|\epsilon - \epsilon_\phi(h_{x,t}^i, t, h_c^i, z_{x,0}^i)\|^2 \quad (2)$$

where  $h_{x,t}^i$  is the diffused local latent representation of the shape  $x^i$  after  $t$  diffusion steps,  $h_c^i$  is the local representation of the corresponding conditioner  $c^i$ ,  $z_{x,0}^i$  is the clean global representation of  $x^i$ ,  $\epsilon$  is the actual noise, and  $\epsilon_\phi$  is the noise predicted by the model. The fixed diffusion variances are defined using a linear scheduler for both models. Note that the latent encodings of the conditioner ( $z_c, h_c$ ) are only used to extract features that are embedded into the diffusion models to guide denoising but they are not diffused. The global DDPM was implemented as a ResNet with 8 squeeze-and-excitation blocks whereas the local DDPM used the same architecture as the CGNet. The PointNet used for extracting global features in CGNet was removed and the global representation of the complete shape generated by the global DDPM was used as global features.

Both models used a 256-dimensional time embedding and 1000 diffusion steps. The dropout of the ResNet layers was set to 0.2. Different from the baseline CGNet, the ReLU activation function is replaced by Swish [32]. Based on the feature size of the local latent representations, the number of the partial input features was set to 4 and the feature dimension of the output was set to 7. The DDPMs were trained in parallel using Adam optimizer with a batch size of 10 and a learning rate of  $2 \times 10^{-4}$  for 16000 epochs.

At inference, the suboptimal shape  $c$  is encoded into its latent representations ( $z_c, h_c$ ), and two noisy inputs  $z_{x,T}$  and  $h_{x,T}$  are sampled from a normal Gaussian distribution. First, the reverse diffusion process is performed on  $z_{x,T}$  using the global DDPM to obtain a clean global representation  $z_{x,0}$ . Later, the local DDPM is used to run the reverse diffusion process on  $h_{x,T}$  to obtain a clean local representation  $h_{x,0}$  using both  $h_c$  and the generated  $z_{x,0}$  as conditions. Finally, the resulting representations are decoded back to the original space via the VAE’s decoder.

### E. Point Cloud Post-Processing

The output of the generative model tends to be sparse and noisy, which negatively impacts the surface reconstruction. This was addressed by a point cloud post-processing pipeline. Initially, each point cloud is re-normalized to the original scale. Subsequently, smoothing is performed using the moving least squares algorithm. Densification follows, where new points are added under the assumption that points within a local neighborhood are within a specified distance of each other; if any neighbor exceeds this target distance, the connecting edge is divided, and a new point is inserted at the midpoint. This process involves a single iteration with a target distance of 10 mm and a neighborhood size of 10 points. Finally, outlier removal is conducted, eliminating points with fewer than 5 neighbors within a 15 mm radius.

### F. Surface Reconstruction

Since the goal is to generate organs for computational phantoms that are usually represented as polygon meshes, we applied a deep implicit model for point-cloud-to-mesh reconstruction (pc2mesh) from the Point-E framework [33]. Based on the input point clouds, this model uses an encoder-decoder Transformer architecture to predict the signed distance functions. The mesh is obtained by applying marching cubes on the signed distance function map. The pre-trained weights were used with a grid size of  $128 \times 128 \times 128$  and a batch size of 1024 points. Point clouds were normalized to  $[-0.5, 0.5]$ .

## III. RESULTS

Shape refinement was evaluated using two metrics: Chamfer distance (CD) and the Hausdorff distance (HD). These metrics collectively assess the completeness and geometric accuracy between the generated shapes and the reference shapes.

### A. 3D Shape Refinement

The point clouds in the test set were refined using both CGNet and CLAP. The resulting point clouds of both model were post-processed as described in section II-E, then the Point-E pc2mesh model was used to generate the polygon meshes. To evaluate the performance, we sampled points from the mesh surfaces and computed CD and HD between the generated and the reference meshes. The results are summarized in table II. Fig 3 shows examples of refined large intestine point clouds using both models. Examples of the post-processed point clouds and the corresponding reconstructed meshes are shown in Fig. 4.

Model	CD ↓	HD ↓
Initial	1400 ± 2620	84.22 ± 58
CGNet	463 ± 871	57.13 ± 32
CLAP	<b>409 ± 716</b>	<b>56.43 ± 31</b>

TABLE II: Shape refinement results after surface reconstruction. Initial condition was synthesized using intentionally under-trained segmentation. Arrows in the header row indicate desired direction of metric, best result for each metric are shown in boldface.

Compared to the starting point, both CGNet and our latent conditional point-diffusion model showed significant improvements for CD and HD (paired t-test,  $p < 0.001$ ). Our model significantly outperformed CGNet by 14.0% (paired t-test,  $p < 0.05$ ) in CD indicating better handling of local errors and improved alignment with reference shapes. Although the 1.3% improvement in HD over the baseline is statistically insignificant, the visual quality improvement in our model compared to CGNet is noticeable. Additionally, our proposed method demonstrates higher stability and robustness, as indicated by lower standard deviation for both metrics. Our method accurately captures the overall distribution of large intestine shapes, producing anatomically acceptable results. It effectively completes missing parts and eliminates false positives in certain scenarios. Visual inspection reveals that

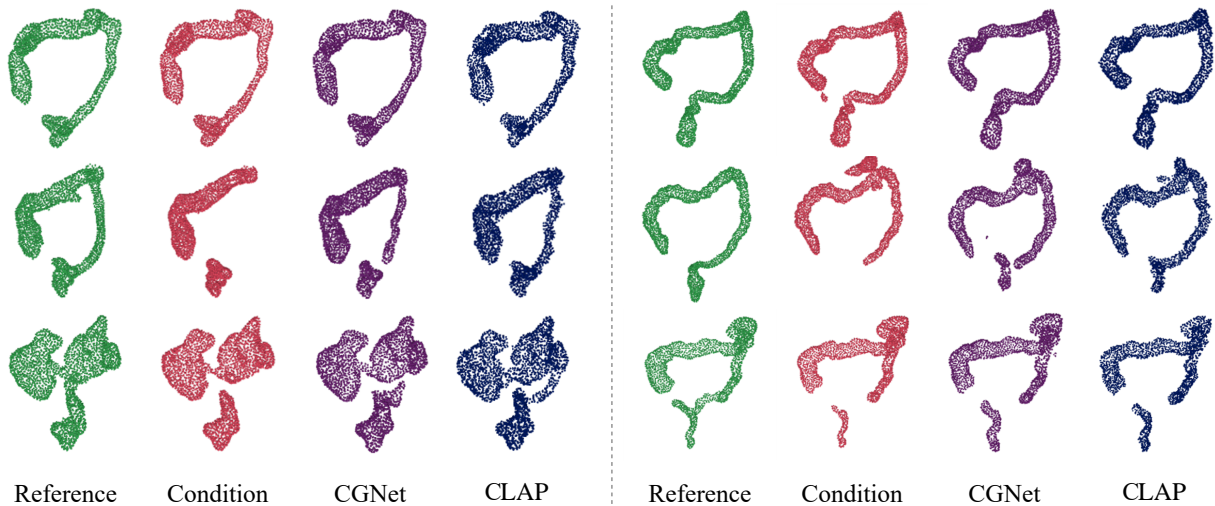


Fig. 3: Examples of the shape refinement results. Initial inputs are also used as condition for both CGNet and CLAP.

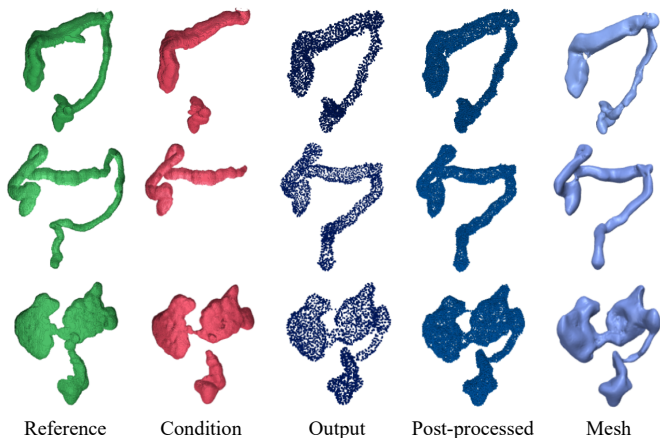


Fig. 4: Example CLAP results of post-processed point clouds and the corresponding reconstructed meshes.

the post-processed point clouds exhibit smoother and denser characteristics compared to the raw ones. The reconstructed meshes exhibit high quality and preserve fine details. In fact, they are less affected by discretization compared to the reference meshes generated from the binary segmentation masks. However, the model faces challenges in removing adjacent or attached false positives but often combines them with correct segments, creating a more plausible connected representation of the large intestine. Occasionally, the model fails to connect organ segments.

It is worth mentioning that the metrics demonstrate a large standard deviation, primarily due to the high contrast in case severity within the test set which encompasses both optimally shaped samples as well as challenging cases. As illustrated in Figure 5, critical scenarios with larger defects exhibit notable enhancements in metric values compared to less severe cases. This trend implies that the average metrics tend to be dominated by cases featuring smaller local defects since they are more abundant in our test set. Consequently,

this prevalence contributes to lower differences between the average metrics of the results and the initial shapes.

### B. TotalSegmentator Refinement

Following the assessment of our proposed pipeline on synthetic data, we proceeded to evaluate its real-world efficacy. Initially, segmentation masks of the large intestine were generated using TotalSegmentator. A set of 20 shapes (comprising 8 CAP and 12 PET/CT scans) were selected based on visual segmentation defects. Subsequently, these masks were manually refined by a physician, thereby creating reference standard masks. The refinement results were compared to the reference standard in Table III; visual examples are in fig. 6.

Model	CD ↓	HD ↓
TotalSeg	571 ± 929	93.97 ± 137
TotalSeg+CGNet	313 ± 543	74.81 ± 131
TotalSeg+CLAP	<b>230 ± 346</b>	<b>72.46 ± 132</b>

TABLE III: Shape refinement results on TotalSegmentator cases

The results demonstrate noticeable improvement of the proposed method in refining the large intestine’s surface compared to the segmentation results of TotalSegmentator. On average, we achieved a 62.32% improvement in CD and a 2.15% improvement in HD, outperforming CGNet in both metrics. The qualitative evaluation confirms that the observations made on the synthetic set (accurate distribution modeling, noise elimination in certain cases, and failure scenarios) are consistent with real-world cases.

### C. Ablation Study

The results reported in this section are obtained on the synthetic test set consisting of 112 cases.

1) *Latent Space Smoothness Impact*: During VAE training, the KL divergence weights of the loss function are gradually increased, leading the latents  $p(z_s)$  and  $p(h_s)$  to converge

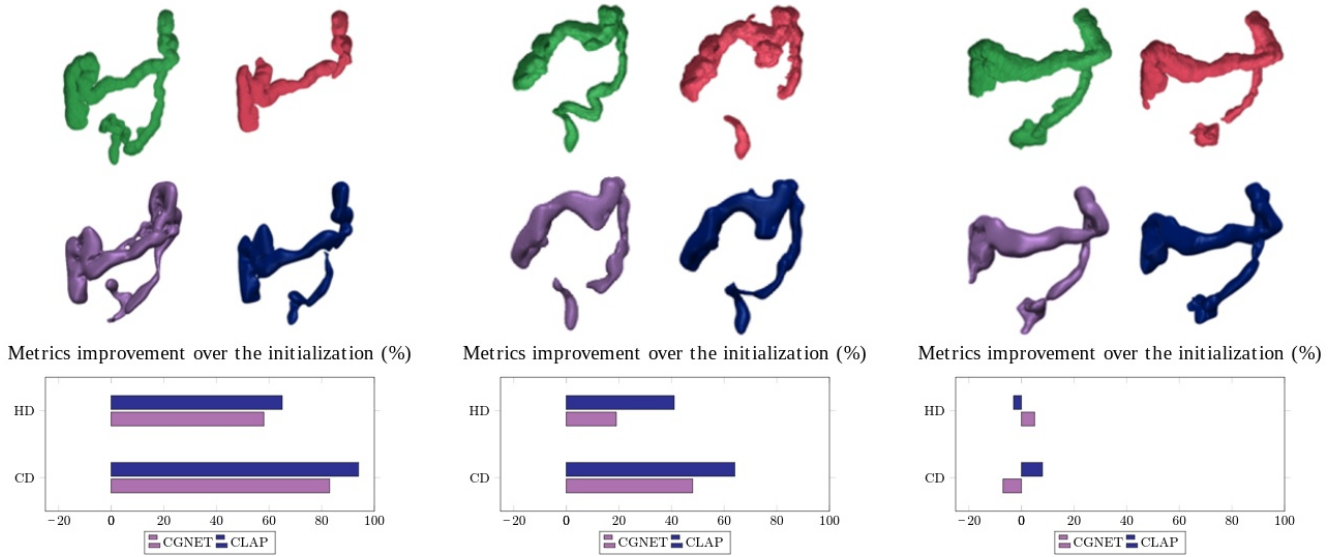


Fig. 5: Improvement for the metrics (CD and HD) relative to the initialization, longer positive bars are better. Difference is larger for cases with larger defects (Left and Middle) compared to cases with small defects (Right).

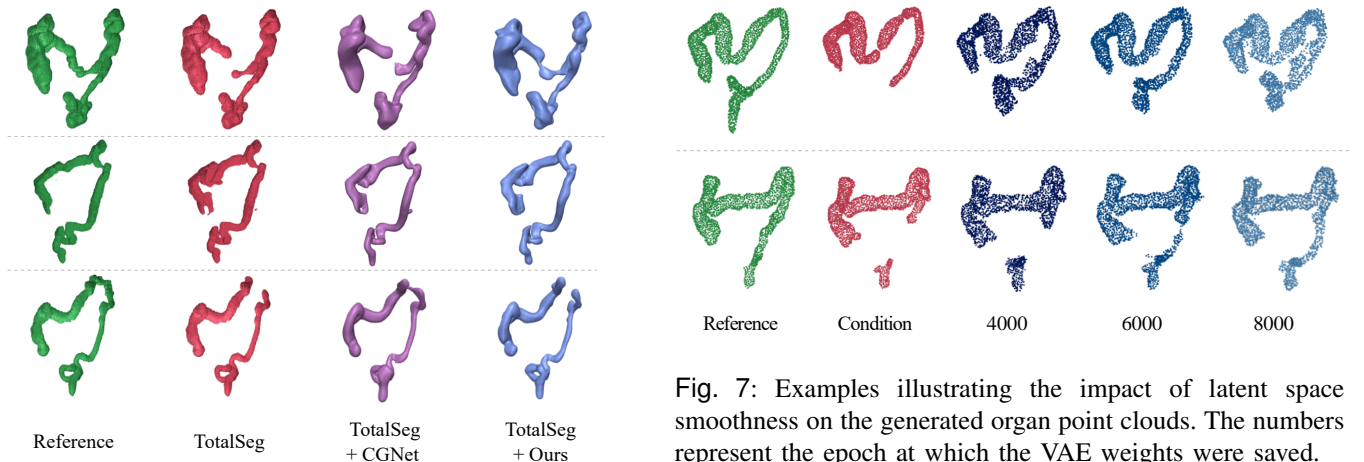


Fig. 6: Examples of TotalSegmentator’s outputs and their refinement results.

towards a standard Gaussian. This results in smoother and more regular latent spaces but increases reconstruction error. To evaluate the impact of VAE weights on the generation process, three latent DDPMs were trained using the VAE weights saved at epochs 4000, 6000, and 8000, respectively. Generation metrics on raw point clouds are presented in Table IV, and example shapes generated using the different models are shown in Fig 7.

The model trained with VAE weights from epoch 6000 outperformed the others in terms of CD, while the model trained with weights from epoch 8000 achieved the lowest HD. Qualitative evaluation showed that extending VAE training time (smoothing the latent space) improved the shape distribution modeling, resulting in more compact and connected organs. However, the reconstruction quality decreased, leading to noisier shapes. Overall, using VAE weights from epoch

Fig. 7: Examples illustrating the impact of latent space smoothness on the generated organ point clouds. The numbers represent the epoch at which the VAE weights were saved.

#Epochs	CD ↓	HD ↓
4000	422 ± 847	55.99 ± 32
6000	<b>388 ± 681</b>	56.44 ± 31
8000	411 ± 821	<b>54.25 ± 32</b>

TABLE IV: Experimental results on latent space smoothness impact on the generated organ point clouds.

6000 balances the trade-off between latent space smoothness and the reconstruction performance.

2) *Post-processing*: To assess the impact of the proposed post-processing pipeline, we generated meshes using both the raw and the post-processed point clouds. Examples of the generated meshes from the raw and post-processed clouds are illustrated in Fig 8.

Prior to post-processing, the average CD was  $427 \pm 837$ , with an HD of  $54.07 \pm 32$ . Following post-processing, the CD increased slightly to  $431 \pm 849$ , while the HD remained stable at  $54.05 \pm 32$ . While the performance metrics do not exhibit a substantial difference, the qualitative evaluation highlights the benefits of post-processing. The meshes generated after post-

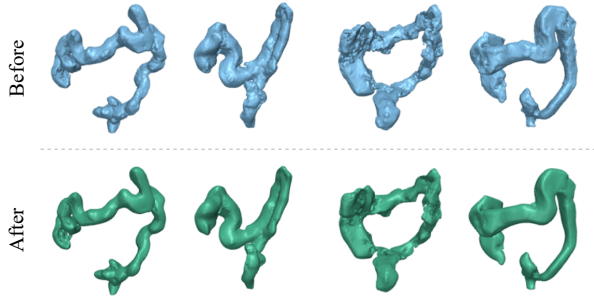


Fig. 8: Examples illustrating the impact of post-processing on the reconstructed meshes.

processing are smoother and suffer fewer holes and noise along their surfaces, which is more compatible with the anatomy of the large intestine’s walls primarily consisting of soft tissues.

#### IV. DISCUSSION

In this study, we leveraged geometric deep learning and denoising diffusion to refine CT segmentation masks, specifically for the challenging organ of the large intestine. Current volumetric segmentation models often exhibit multiple issues such as missing parts or spurious noise. Our approach treated this as a conditional point cloud generation task, using a hierarchical variational autoencoder for encoding shapes into a smoother latent space consisting of a global and a local representation. Two denoising diffusion models were then trained in this latent space to perform point cloud refinement. After decoding back to the original space, post-processing was performed by using a deep implicit model to reconstruct the refined point cloud into smooth meshes.

Compared to CGNet, our method showed that training the denoising diffusion models in a hierarchical latent space improved the modeling of shape distributions, particularly in capturing fine details. Our method effectively handled false positives, while CGNet sometimes produced anatomically inaccurate details, such as introducing small branches in the colon. The study on the impact of latent space smoothness showed that models trained in smoother spaces preserved the organ’s anatomy more accurately. However, it’s important to note the differences in point cloud density and uniformity between CGNet and our latent model, which our post-processing and mesh reconstruction methods effectively resolved.

Unlike the point classification network [18] used to eliminate background points in the segmentation result, our method utilizes generative deep learning. This enabled our model to generate new parts and complete shapes. In a previous study, the PVD architecture [23] was adopted for generating skull implants [27]. Their method assumed a partial shape that is entirely contained within the target shape and kept it fixed throughout the diffusion process. This would be impractical for our task, because the conditioner may contain noise and fragments of other organs, leaving false positive points in the output. To overcome this issue, we employed the CGNet architecture [25] which does not fix the partial shape but rather extracts its features to guide the generation. This strategy successfully eliminated noisy components from the masks.

We applied our pipeline to outputs generated by TotalSegmentator, a well-known model that was trained on one of the largest public imaging datasets. There were improvements in the surface representation performance. Additionally, the qualitative evaluation confirmed the consistency of our results, indicating the faithfulness of our synthetic dataset to actual segmentation outputs and our model’s generalizability to new cases.

#### A. Limitations

While our method demonstrates promise for large intestine segmentation refinement, it has limitations. The model faces difficulties in eliminating false positives closely adjacent or attached to the actual segments of the organ, with PointNet’s layers sometimes misclassifying these points as true positives. Additionally, it is still challenging to connect large gaps between segments, especially near the rectosigmoid junction, and may produce anatomically inaccurate shapes for complex inputs. These errors are expected since the size of the dataset used to train the model is very small compared to common computer vision datasets typically used for this task such as ShapeNet [34] which includes over 50000 shapes. Increasing the training set size and pre-training the model on larger sets may address these issues. Moreover, the generated shapes sometimes misalign with the reference standard and intersect with neighboring organs, which impacts the ability to create consistent computational phantoms with multiple organs. The current model relies only on the provided partial shape, lacking contextual information about surrounding anatomy.

#### B. Future Work

For future model improvements, we propose: (1) Refining CGNet’s hyperparameters and attention modules to better distinguish between true and false positives. (2) Increasing data diversity through more CT scans and optimizing data augmentation. (3) Using landmarks from neighboring organs to condition the generative models to avoid intersections and improve shape accuracy. (4) Optimizing the landmarks extraction technique for a more generalizable synthesis approach, potentially generating new organs from scratch without the segmentation initialization. (5) Enhancing mesh reconstruction by fine-tuning the Point-E model or modifying the VAE decoder to output signed distance functions. These steps aim to eliminate false positives, diversify the dataset, and improve mesh reconstruction quality.

#### V. CONCLUSIONS

In this paper, we have introduced an end-to-end pipeline designed to refine the 3D shapes of the large intestine, significantly augmenting surface reconstruction quality from initially suboptimal segmentations. Leveraging geometric deep learning and denoising diffusion probabilistic models, our method solves a conditional point cloud generation task within a hierarchical latent space. Our experimental results demonstrate both quantitatively and qualitatively compelling improvements, showcasing refined 3D shapes characterized by



enhanced surface reconstruction and anatomical precision. By focusing on the large intestine as a case study, our findings underscore the high potential of these advanced techniques, which hold promise for broader applications in computational phantoms and beyond.

## VI. REFERENCES

- [1] W. Segars, J. Bond, J. Frush, S. Hon, C. Eckersley, C. H. Williams, J. Feng, D. J. Tward, J. Ratnanather, M. Miller *et al.*, "Population of anatomically variable 4d xcat adult phantoms for imaging research and optimization," *Medical physics*, vol. 40, no. 4, p. 043701, 2013.
- [2] J. Y. Hesterman, S. D. Kost, R. W. Holt, H. Dobson, A. Verma, and P. D. Mozley, "Three-dimensional dosimetry for radiation safety estimates from intrathecal administration," *Journal of Nuclear Medicine*, vol. 58, no. 10, pp. 1672–1678, 2017.
- [3] M. Wang, N. Guo, G. Hu, G. El Fakhri, H. Zhang, and Q. Li, "A novel approach to assess the treatment response using gaussian random field in pet," *Medical Physics*, vol. 43, no. 2, pp. 833–842, 2016.
- [4] W. P. Segars, G. Sturgeon, S. Mendonca, J. Grimes, and B. M. Tsui, "4d xcat phantom for multimodality imaging research," *Medical physics*, vol. 37, no. 9, pp. 4902–4915, 2010.
- [5] C. Lee, D. Lodwick, D. Hasenauer, J. L. Williams, C. Lee, and W. E. Bolch, "Hybrid computational phantoms of the male and female newborn patient: Nurbs-based whole-body models," *Physics in Medicine & Biology*, vol. 52, no. 12, p. 3309, 2007.
- [6] Y. Liu, Y. Lei, Y. Fu, T. Wang, X. Tang, X. Jiang, W. J. Curran, T. Liu, P. Patel, and X. Yang, "Ct-based multi-organ segmentation using a 3d self-attention u-net network for pancreatic radiotherapy," *Medical physics*, vol. 47, no. 9, pp. 4316–4324, 2020.
- [7] A. D. Weston, P. Korfiatis, K. A. Philbrick, G. M. Conte, P. Kostandy, T. Sakinis, A. Zeinoddini, A. Boonrod, M. Moynagh, N. Takahashi *et al.*, "Complete abdomen and pelvis segmentation using u-net variant architecture," *Medical physics*, vol. 47, no. 11, pp. 5609–5618, 2020.
- [8] J. Wasserthal, M. Meyer, H.-C. Breit, J. Cyriac, S. Yang, and M. Segeroth, "Totalsegmentator: robust segmentation of 104 anatomical structures in ct images," *arXiv preprint arXiv:2208.05868*, 2022.
- [9] J. J. Cerrolaza, M. L. Picazo, L. Humbert, Y. Sato, D. Rueckert, M. Á. G. Ballester, and M. G. Linguraru, "Computational anatomy for multi-organ analysis in medical imaging: A review," *Medical image analysis*, vol. 56, pp. 44–67, 2019.
- [10] C. Wang, Z. Cui, J. Yang, M. Han, G. Carneiro, and D. Shen, "Bowelnnet: Joint semantic-geometric ensemble learning for bowel segmentation from both partially and fully labeled ct images," *IEEE Transactions on Medical Imaging*, 2022.
- [11] O. Ronneberger, P. Fischer, and T. Brox, "U-net: Convolutional networks for biomedical image segmentation," in *Medical Image Computing and Computer-Assisted Intervention—MICCAI 2015: 18th International Conference, Munich, Germany, October 5–9, 2015, Proceedings, Part III 18*. Springer, 2015, pp. 234–241.
- [12] J. Yang, U. Wickramasinghe, B. Ni, and P. Fua, "Implicitatlas: learning deformable shape templates in medical imaging," in *Proceedings of the IEEE/CVF Conference on Computer Vision and Pattern Recognition*, 2022, pp. 15 861–15 871.
- [13] A. Raju, S. Miao, D. Jin, L. Lu, J. Huang, and A. P. Harrison, "Deep implicit statistical shape models for 3d medical image delineation," in *Proceedings of the AAAI Conference on Artificial Intelligence*, vol. 36, no. 2, 2022, pp. 2135–2143.
- [14] L. Bai, Y. Zhao, M. Elhousni, and X. Huang, "Depthnet: Real-time lidar point cloud depth completion for autonomous vehicles," *IEEE Access*, vol. 8, pp. 227 825–227 833, 2020.
- [15] J. Varley, C. DeChant, A. Richardson, J. Ruales, and P. Allen, "Shape completion enabled robotic grasping," in *2017 IEEE/RJSJ international conference on intelligent robots and systems (IROS)*. IEEE, 2017, pp. 2442–2447.
- [16] C. R. Qi, H. Su, K. Mo, and L. J. Guibas, "Pointnet: Deep learning on point sets for 3d classification and segmentation," in *Proceedings of the IEEE conference on computer vision and pattern recognition*, 2017, pp. 652–660.
- [17] A. Jana, H. M. Subhash, and D. Metaxas, "Automatic tooth segmentation from 3d dental model using deep learning: a quantitative analysis of what can be learnt from a single 3d dental model," in *18th International Symposium on Medical Information Processing and Analysis*, vol. 12567. SPIE, 2023, pp. 42–51.
- [18] F. Balsiger, Y. Soom, O. Scheidegger, and M. Reyes, "Learning shape representation on sparse point clouds for volumetric image segmentation," in *Medical Image Computing and Computer Assisted Intervention—MICCAI 2019: 22nd International Conference, Shenzhen, China, October 13–17, 2019, Proceedings, Part II 22*. Springer, 2019, pp. 273–281.
- [19] Y. Li, R. Bu, M. Sun, W. Wu, X. Di, and B. Chen, "Pointcnn: Convolution on x-transformed points," *Advances in neural information processing systems*, vol. 31, 2018.
- [20] J. Ho, A. Jain, and P. Abbeel, "Denoising diffusion probabilistic models," *Advances in Neural Information Processing Systems*, vol. 33, pp. 6840–6851, 2020.
- [21] J. Zhang, S. Jayasuriya, and V. Berisha, "Restoring degraded speech via a modified diffusion model," *arXiv preprint arXiv:2104.11347*, 2021.
- [22] A. Lugmayr, M. Danelljan, A. Romero, F. Yu, R. Timofte, and L. Van Gool, "Repaint: Inpainting using denoising diffusion probabilistic models," in *Proceedings of the IEEE/CVF Conference on Computer Vision and Pattern Recognition*, 2022, pp. 11 461–11 471.
- [23] L. Zhou, Y. Du, and J. Wu, "3d shape generation and completion through point-voxel diffusion," in *Proceedings of the IEEE/CVF International Conference on Computer Vision*, 2021, pp. 5826–5835.
- [24] X. Zeng, A. Vahdat, F. Williams, Z. Gojcic, O. Litany, S. Fidler, and K. Kreis, "Lion: Latent point diffusion models for 3d shape generation," in *Advances in Neural Information Processing Systems*, 2022.
- [25] Z. Lyu, Z. Kong, X. Xu, L. Pan, and D. Lin, "A conditional point diffusion-refinement paradigm for 3d point cloud completion," *arXiv preprint arXiv:2112.03530*, 2021.
- [26] C. R. Qi, L. Yi, H. Su, and L. J. Guibas, "Pointnet++: Deep hierarchical feature learning on point sets in a metric space," *Advances in neural information processing systems*, vol. 30, 2017.
- [27] P. Friedrich, J. Wolleb, F. Bieder, F. M. Thieringer, and P. C. Cattin, "Point cloud diffusion models for automatic implant generation," *arXiv preprint arXiv:2303.08061*, 2023.
- [28] F. Isensee, P. F. Jaeger, S. A. Kohl, J. Petersen, and K. H. Maier-Hein, "nnu-net: a self-configuring method for deep learning-based biomedical image segmentation," *Nature methods*, vol. 18, no. 2, pp. 203–211, 2021.
- [29] W. E. Lorensen and H. E. Cline, "Marching cubes: A high resolution 3d surface construction algorithm," *ACM siggraph computer graphics*, vol. 21, no. 4, pp. 163–169, 1987.
- [30] C. Yuksel, "Sample elimination for generating poisson disk sample sets," in *Computer Graphics Forum*, vol. 34, no. 2. Wiley Online Library, 2015, pp. 25–32.
- [31] Z. Liu, H. Tang, Y. Lin, and S. Han, "Point-voxel cnn for efficient 3d deep learning," *Advances in Neural Information Processing Systems*, vol. 32, 2019.
- [32] P. Ramachandran, B. Zoph, and Q. V. Le, "Searching for activation functions," *arXiv preprint arXiv:1710.05941*, 2017.
- [33] A. Nichol, H. Jun, P. Dhariwal, P. Mishkin, and M. Chen, "Point-e: A system for generating 3d point clouds from complex prompts," *arXiv preprint arXiv:2212.08751*, 2022.
- [34] A. X. Chang, T. A. Funkhouser, L. J. Guibas, P. Hanrahan, Q.-X. Huang, Z. Li, S. Savarese, M. Savva, S. Song, H. Su, J. Xiao, L. Yi, and F. Yu, "Shapenet: An information-rich 3d model repository," *ArXiv*, 2015.